4 Application to Hydraulic Fracturing Data

In this chapter the location method as well as receiver fidelity tests are applied to data from a hydraulic fracturing experiment at the Carthage Cotton Valley tight gas field. The Carthage Cotton Valley field is located in Panola County, East Texas, USA (see Figure 4.1). It is one of the top producing gas fields of Texas and every effort is made to maximize the gas production. A maximation of production can be achieved by increasing the flow of fluids/gas to the well by connecting many pre-existing fractures in the reservoir rock with a larger fracture. Such a large fracture starts at the production well and extends out into the reservoir formation for several tens to several hundred meters. This reservoir stimulation technique is called *hydraulic fracturing* and is commonly used for production well completion of the low-permeability reservoirs of the Cotton Valley formation (Wescott, 1983). For the hydraulic fracturing specially engineered fluids are pumped at high pressure and high pumping rate into the formation. The high fluid pressure exceeds the rock strength and opens a fracture into the formation or reactives preexisting fractures as described in section 2.1. Proppant, such as sand grains of a particular size, is added to the treatment fluid to keep the fracture open when the pressure is released after the pumping stop (Sheriff, 2002). The process of opening and reactivating fractures creates seismic emissions in the form of small magnitude earthquakes. The spatial distribution of these microearthquakes is related to the size of the stimulated reservoir volume and hence can be used to image the fracture, map its geometry and estimate the success of the treatment (see, e.g., House, 1987; Warpinski, 1994; Shapiro et al., 1997).

In 1997, an industry consortium of operators, service companies, government agencies and national laboratories was formed to investigate hydraulic fracture treatments in more detail (Walker Jr., 1997). The major aim was to determine key geometrical attributes of hydraulic fractures such as height, length and azimuth as well as the optimization of hydraulic fracture designs. For the experiment three wells have been utilized (see Figure 4.2). As given in Walker Jr. (1997) the fracture

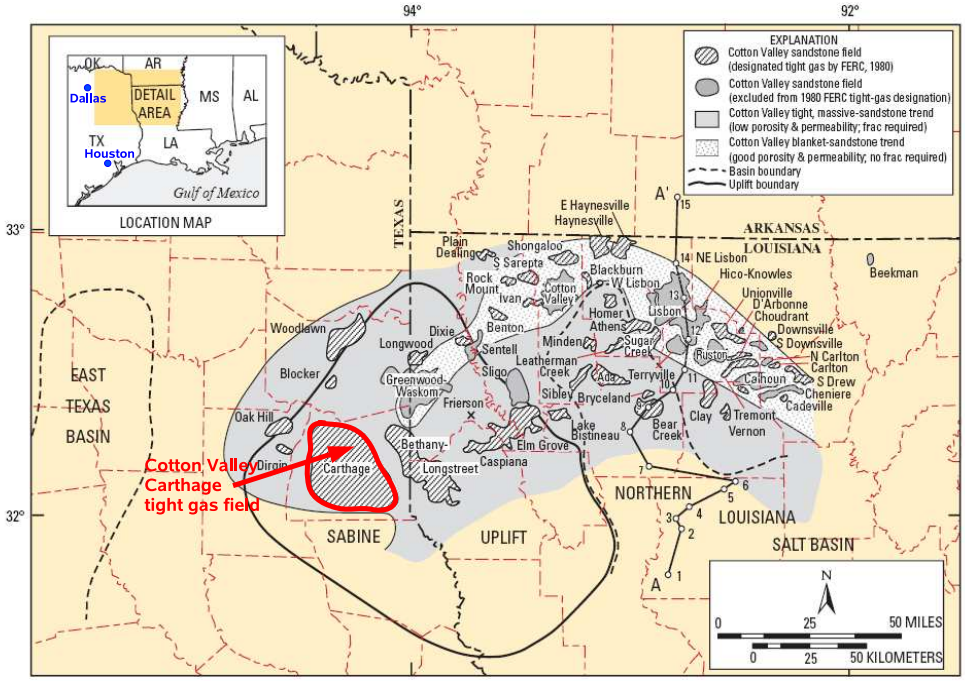

Figure 4.1: Map of northeast Texas and northern Louisiana (modified after Dyman and Condon (2006)). Fields excluded from ”tight-gas” designation by the Federal Energy Regulatory Commission (FERC) in 1980 are shown in darker gray shading. The abbreviation ”frac” indicates ”fracture-stimulation treatment”. Light grey and shaded fields produce hydrocarbons from Cotton Valley Group sandstones.

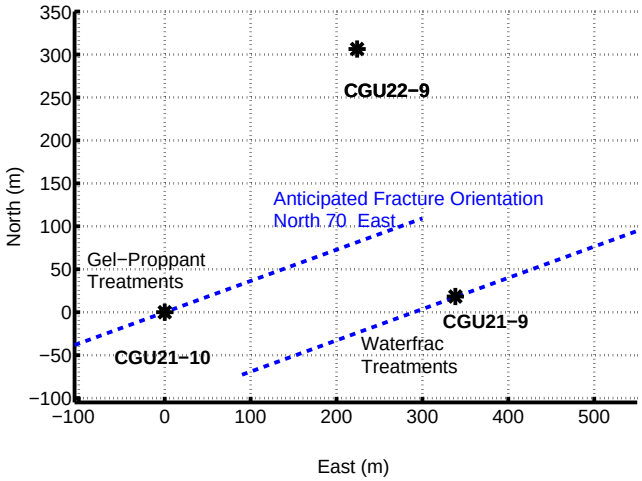

Figure 4.2: Well geometry and the expected fracture orientation after Walker Jr. (1997).

azimuth was approximated to be North 70° East. Therefore the two monitoring wells were placed in a way they would straddle one wing of the expected fracture of the experiments phase I. The experiment consisted of four project phases. In phase I the hydraulic stimulation was performed in the Carthage Gas Unit (CGU) 21-10 using gel-proppant for injection. The wells CGU 22-9 and CGU 21-9 were used as monitoring wells. In phase II CGU 21-9 became the treatment well for the waterfrac experiment and only well CGU 22-9 was used as a monitoring well. The details are summarized in Table 4.1. In phase III waterfrac evaluation was conducted in well CGU 22-9 using wireline-deployed downhole tiltmeter arrays. The aim of phase IV was further analysis on the hydraulic fractures performed in the CGU 21-10 and CGU 21-9 including determination of fracture length, height, direction, asymmetry and source parameters.

Fracture operation 1997	Depth interval (m)	Total Perforation (m)	Treatment	Monitoring well
May 12, CGU 21-10 Phase 1, Stage 1	2932 - 2938	6	Gel Proppant	CGU 21-9 CGU 22-9
May 14, CGU 21-10 Phase 1, Stage 2	2757 - 2838	24	Gel Proppant	CGU 21-9 CGU 22-9
May 16, CGU 21-10 Phase 1, Stage 3	2615 - 2696	24	Gel Proppant	CGU 21-9 CGU 22-9
July 14, CGU 21-09 Phase 2, Stage 1	2746 - 2763	9	Waterfac	CGU 22-9
July 16, CGU 21-09 Phase 2, Stage 2	2663 - 2687	12	Waterfrac	CGU 22-9
July 18, CGU 21-09 Phase 2, Stage 3	2607 - 2643	12	Waterfrac	CGU 22-9

Table 4.1: Details of the different hydraulic fracturing experiments in the Cotton Valley formation after Rutledge et al. (2004).

4.1 Geological settings

The Cotton Valley sandstone formation is a subsurface sequence of Late Jurassic sandstones, shales as well as carbonates and extends from northeast Texas to north Louisiana (see Figure 4.1). For the particular field investigated in this study the top of the Cotton Valley section is about 2600 m deep and approximately 325 meters thick (Rutledge and Phillips, 2003). Detailed well log information of the Cotton Valley sandstone formation obtained in well CGU 21-10 are shown in Figure 4.3. Overlaying the Cotton Valley formation is the Travis Peak formation, another thick ($\pm$ 450-600m) interval of productive, low-permeability gas sands interbedded with mudstones. Both formations are believed to be within a normal-faulting stress regime with minimal horizontal stress oriented north-northwest (Rutledge and Phillips (2003)).

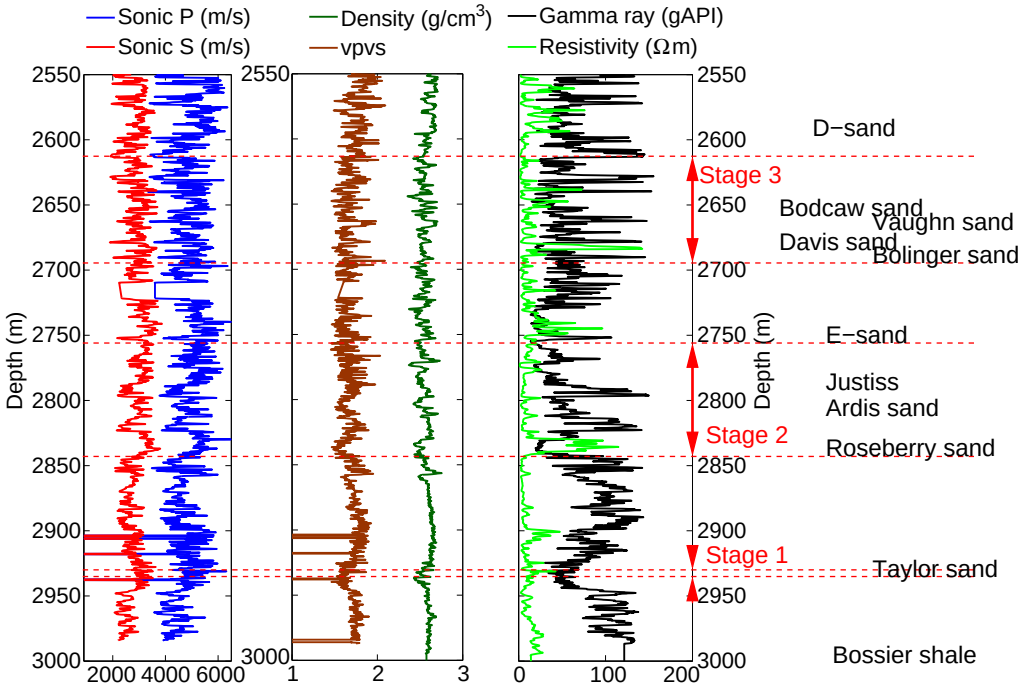

Figure 4.3: Well logs from CGU 21-10: Sonic logs, VpVs-ratio, Density log, Resistivity and Gamma ray log (gAPI = American Petroleum Institute gamma ray units).

The diagenetic history of the Cotton Valley formation was mainly controlled by wave dominated, shallow marine depositional environments (Wescott, 1983). Due to a series of marine and lagoonal deposits the Cotton Valley interval includes very fine-grained sandstones, siltstones, shales and limestones. Shale laminations are extensive, resulting in small sand members ranging in thickness from a few centimeters to 3 to 5 meters (Meehan and Verma (1994)). The highly altering gamma ray log shown in Figure 4.3 reflects the lamination where high gamma ray values are associated with shales and low values with sandstone. Bounding shale laminae are lenticular and discontinuous. Diagenesis in the form of calcite cementation and quartz overgrowth, combined with overburden pressure have significantly reduced porosity and permeability. Sand porosities range from 2 percent to 12 percent with microdarcy-level permeabilities (Meehan and Verma (1994)). With such low porosity and permeability values, gas or fluids do not flow. The production of the hydrocarbons in the Carthage Cotton Valley formation becomes only economical if the formation is fractured to increase the hydraulic conductivity. Hence, the Carthage tight gas field was most suitable to perform hydraulic fracturing experiments.

4.2 The monitoring wells and its instrumentation

The goal of the project was to image a hydraulic fracture stimulation using only wells which fulfilled the nominal 80 acre spacing rules of the actual producing environment. [1] This rule specified a minimum of 1000 ft (305 m) between boreholes and the two monitoring wells utilized for the experiment were located approximately 400 m to the east and northeast of the treatment well (see Figure 4.2).

The aperture of the arrays was designed to accommodate both the passive seismic emissions (induced by the fracture process) and a crosswell tomographic velocity survey (Walker Jr., 1997). The array design was mainly based on the requirements of the planned crosswell tomography which needed wide apertures and consisted of two 2350 ft (716.28 m) long downhole arrays. Both arrays consisted of 48 three-component receivers with 50 ft (15.24 m) spacing (see Figure 4.4).

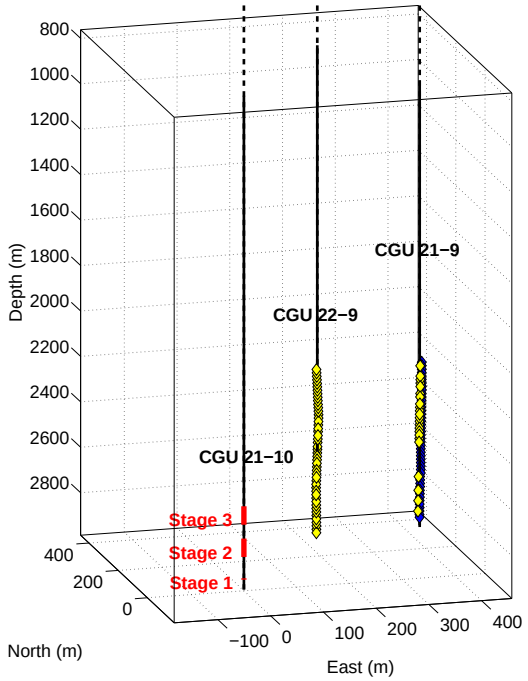

Figure 4.4: Acquisition geometry designed to record passive seismic data as well as crosswell seismic data. The data set analyzed in this thesis did only contain traces of the receivers marked as yellow diamonds. The traces from the receivers marked as blue diamonds were not provided.

Based on experiences from a pilot study in 1994 conducted by Union Pacific Resources in the Carthage Cotton Valley field the dominant frequency of the induced events was expected to be less than 200 Hz. The consortium designed a sensitive and amplified triaxial geophone based on *3 GeoSpace 30 Hz SMC - 1850*

[1] In order to conserve resources and protect correlative rights well spacing rules for a field are established.

geophones. These geophones are operational in all directions, sensitive to sufficient band-width and temperature rated to 200°C, so it could clearly stand the temperature rises that were expected during the cement hydration. Furthermore, the electronics were packed into a stainless steel cylinder with caps to withstand 10000 psi (69 MPa)[2]. Also special cables were designed and manufactured using special insulation to withstand 200°C in the deeper section of the borehole and 135°C in the lower part. *OYO DAS-1 96* channel recorders were used to filter (3 Hz low cut), sample (1000 Hz) and amplify (48 dB) the incoming analog signal. The digital data were passed to a workstation where records of 8 s length were displayed, automatically scanned and visually searched for microseismicity detection. Whenever an event was detected a separate record of approximately 400 ms length was stored to disk.

The following information about the installation of the recording network and the encountered problems are given in Walker Jr. (1997). Additional information and explanations are results of personal communication with people involved in the project like Steven Wolhart (Pinnacle Technologies) and Jim Rutledge (Los Alamos National Laboratory). For deployment of the geophones the pods where strapped to the casing with metal bands and the connectors were covered with protective tape. The advantage of fixing the pods to the casing before deployment is that all geophone assemblies have the same orientation to the casing. Problems occurred during the deployment process in CGU 21-9 between 2140 – 2350 m where a tight spot or bridge was encountered in the open hole. The bottom sonde was damaged passing the tight spot. The whole deployment procedure was slowed but the resistance still increased the more sondes passed the 2350 m mark. Some sondes were subsequently damaged during this process. For reservoir safety reasons the casing needed to be deployed down to the bottom of the Upper Cotton Valley pay interval and as soon as this depth was reached the operator stopped the deployment and cemented the array. Note, that the aimed depth of the array was not reached. Subsequent crosswell check shots performed in the treatment well CGU 21-10 showed that approximately only half of the sondes of array 1 were functioning. Array 2 was deployed as aimed and reached the bottom hole of CGU 22-9. Most of the geophones were functioning after cementation (Walker Jr., 1997) but during the recording operations it was recognized that communication with some sondes was periodically lost.

Even if the geophones were initially deployed with the same orientation to the casing the process of cementation as well as the deployment itself could have displaced the orientation. The orientation was analyzed using a *Rotoscan log* which located an iridium tracer azimuth. The tracer azimuth also provided the determination of absolute geophone orientations. The result of this analysis is shown in Figure 4.5 and details are given in Appendix B.1, Table B.1 and B.2.

[2]It was estimated that the downhole pressure could rise to about 7,600 psi during the cementing process as the cement slurry is supposed to displace the drilling mud.

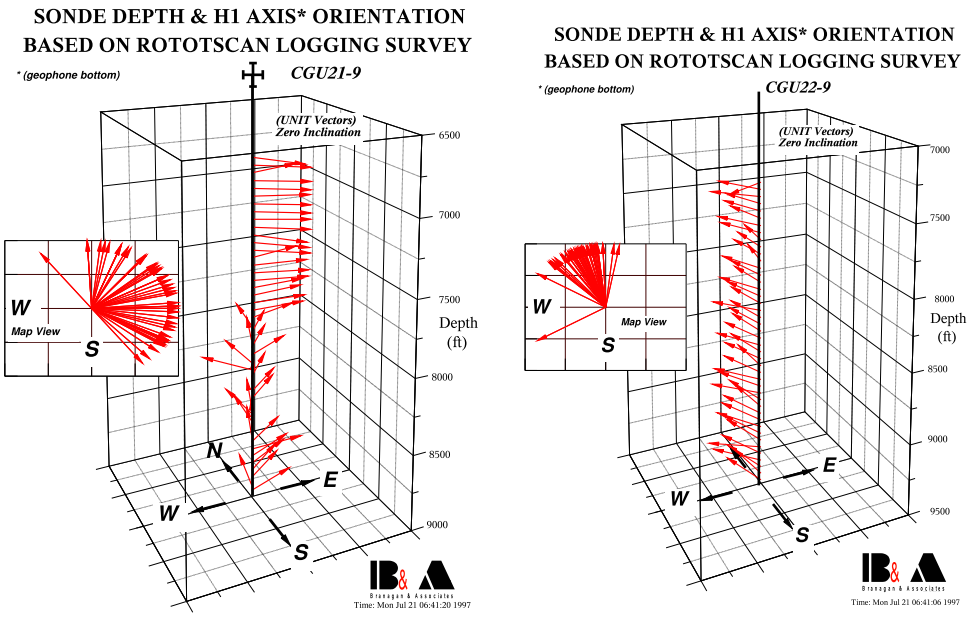

Figure 4.5: Receiver orientation obtained from Rotoscan analysis. Pictures taken from the Cotton Valley Hydraulic Fracture Imaging and Waterfrac Project data supplemental CD.

The iridium tracer pill was glued into a hole on the mount to which the sonde was fixed. For this reason the tracer logs provide rather azimuths of the mount than of the geophone pod and the logs also contained azimuth values of the damaged receivers. The quality of this analysis is difficult to estimate and depends on how good the sonde was fixed. A different analysis using azimuths of incoming check shots (as described in section 3.5) as well as relative azimuths of located microearthquakes was performed by Jim Rutledge (pers. comm., 2004) as well as by the Engineering Seismology Group Inc. (ESG) (Urbancic, 1998) for some receivers in CGU 22-9. The corresponding results can also be found in Appendix B.1, Table B.2. The azimuths obtained from the hodogram based analysis differed up to a maximum of 18 degrees from the *Rotoscan* derived orientations.

4.3 Data analysis and receiver fidelity tests

As mentioned above, problems occurred during the deployment of the receivers. From the 96 cemented receivers 58 receivers had one or more malfunctioning components. In detail, the data set did not contain complete three-component waveforms for 35 receivers in CGU 21-9 and 23 receivers in CGU 22-9. Some of the remaining receivers showed significant differences in the mean noise amplitudes on their three components. For example, Figure 4.6 shows the three-component recordings of twelve receivers in CGU 21-9. It can be seen that some traces (e.g., at receiver 2102, 2107 or 2110) cannot be considered as receivers with

high component fidelity. Similar problems can be observed at some receivers in CGU 22-9 (see Figure 4.7).

The shown differences in the amplitudes / mean noise levels can be caused by differences in the sensitivity or coupling as well as by polarized noise. These factors disturb the polarization as explained in section 3.5. Furthermore, it was shown that a disturbed component fidelity could also lead to misfits in the receiver orientation when hodogram-based methods are used.

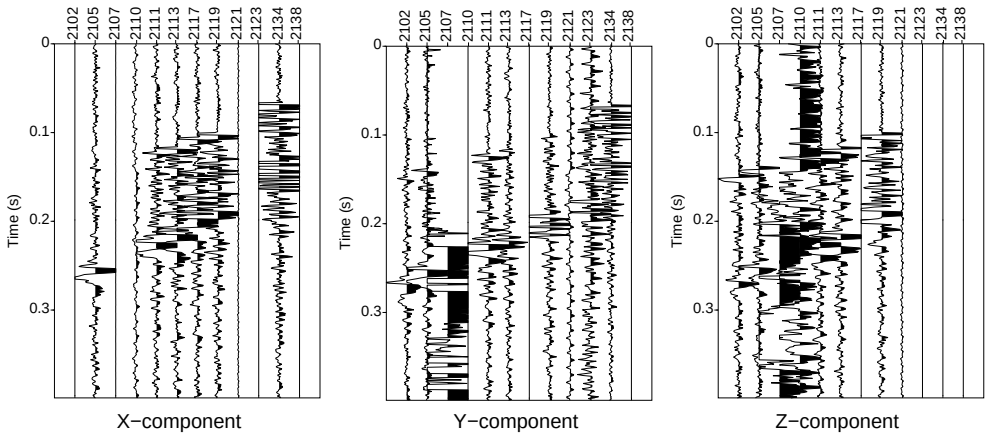

Figure 4.6: Traces of one detected event recorded in CGU 21-9.

In order to distinguish between the different quality levels of the receivers the data have been preprocessed by analysing the component fidelity as described in section 3.5. Six different data files were utilized to estimate component fidelities from mean noise levels. The resulting component fidelity of the receivers in well CGU 21-9 is shown in Figure 4.8. The top plot corresponds to the X-component, the middle plot to the Y-component and the bottom plot to the Z-component, respectively. It can be seen that the fidelity estimates are relatively stable over the six different noise intervals. From the considerations in section 3.5 it follows that 30 % fidelity deviation lead to up to 10 degree misfit in polarization angles if only one component has different fidelity. Of course, the polarization angles become more disturbed if all three components show different fidelity values. It was decided that only receivers with less than 30 % fidelity deviation will be used for further processing. As shown in Figure 4.8 only 4 receivers (indicated by red arrows) fulfilled this threshold in the CGU 21-9 monitoring well. Better results were obtained from CGU 22-9, were 16 receivers passed the fidelity test (see Figure 4.9).

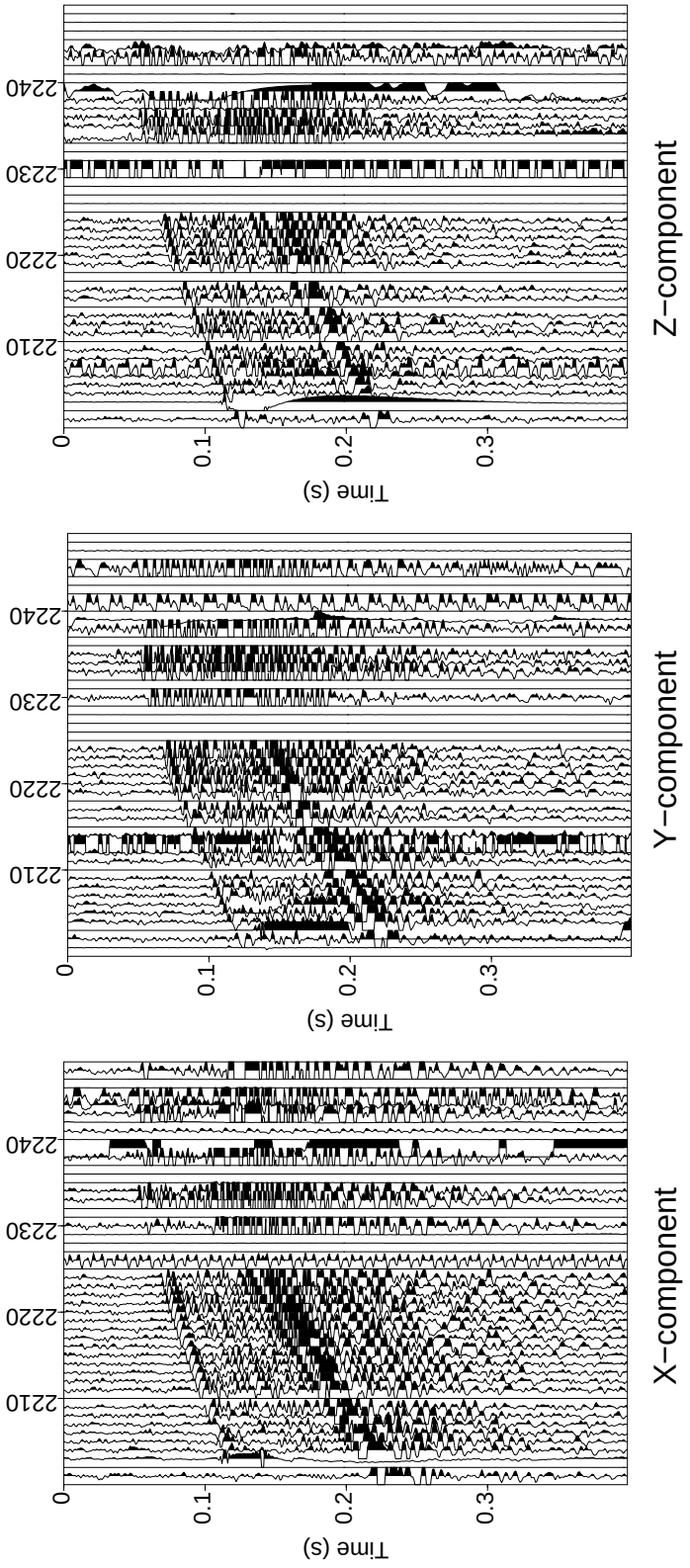

Figure 4.7: Traces of one detected event recorded in CGU 22-9.

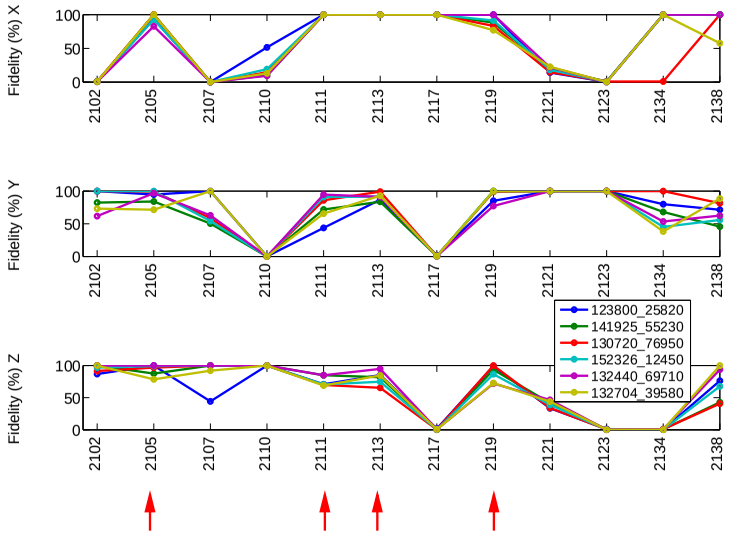

Figure 4.8: Component fidelity of the receivers in CGU 21-9. Four receivers (2105, 2111 2113 and 2119) were used for location.

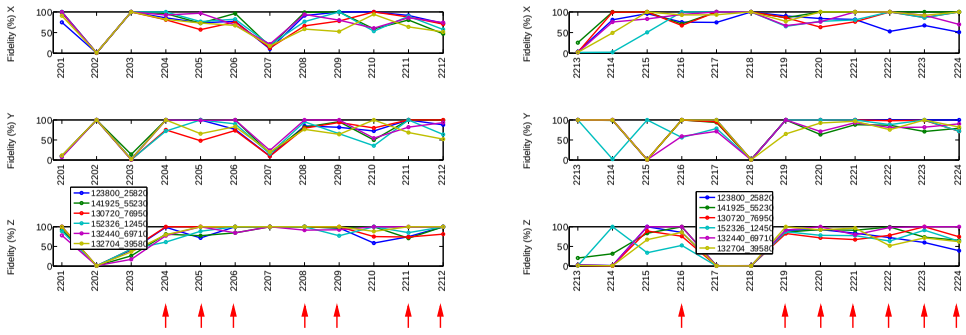

(a) Receiver 1 – 12.

(b) Receiver 13 – 24

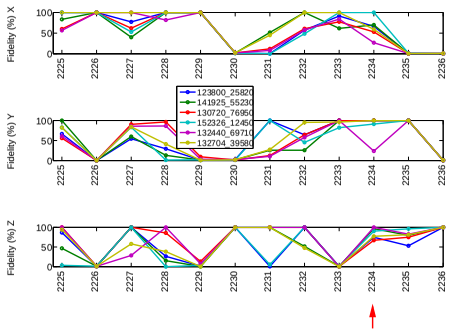

(c) Receiver 25 – 36

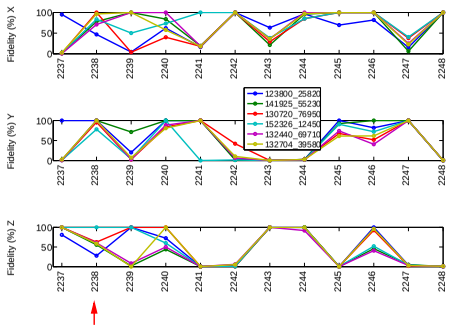

(d) Receiver 37 – 48

Figure 4.9: Component fidelity of the receivers in CGU 22-9. The 16 receivers marked by red arrows were used for location.

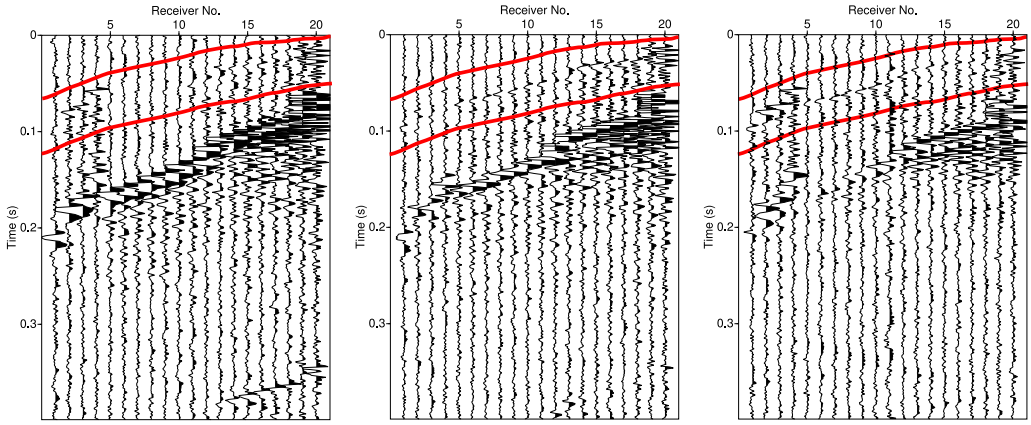

Figure 4.10: Seismograms (recorded at 20 functioning receivers) of a detected event rotated into geographical coordinates. From left: East-, North- and vertical-component. The waveforms around the P-wave onset (within the red marked interval) were used for the location.

4.4 Event location

The traces of these 20 receivers were rotated into the geographical coordinate system using the receiver azimuths provided by J. Rutledge (Los Alamos National Laboratory), ESG (Urbancic, 1998) and the rotoscan analysis. For details see Appendix B.1.

Figure 4.10 shows the waveforms of one detected event. The next step was to identify and to select the P-wave window. As described in section 3.1 STA/LTA ratios, spectrograms and rectilinearity values can be utilized for single receiver detection. As an example the result of the single receiver detection for receiver number 3 is shown in Figure 4.11. The first onset in the STA/LTA ratio at 0.3 s corresponds to the first calculated STA/LTA ratio (the first time sample after the first LTA window) and not to an event. Some of the event files started relatively close to the P-wave onset (as the one shown in Figure 4.10). This means that the traces of especially the lower receivers (in some event files) did not contain sufficiently long intervals of noise to obtain meaningful results from the STA/LTA ratio analysis (see receivers 10-20 in Figure 4.10). For this reason the detection at the lower receivers in CGU 22-9 was only based on spectrograms and rectilinearity values.

Furthermore, polarization consistency tests were performed to check whether the dip and azimuth of the polarization vector was consistent with a P-wave originating from the volume that was expected to be seismically active (600 m x 500 m x 500 m around the injection interval). The investigated parameters are shown in Figure 4.12. At times when high rectilinearity values occur consistent azimuths can be observed. The azimuth values that correspond to the first sharp rectilinearity onset point backward to the treatment well (indicating a P-wave) whereas the

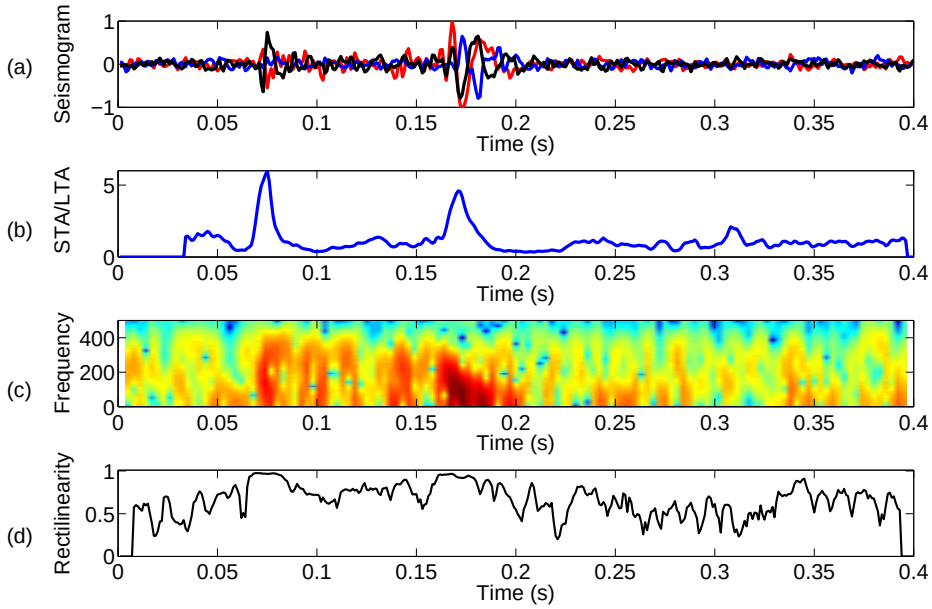

Figure 4.11: Detection of P- and S-waves. (a) 3C traces of the event in Figure 4.10 at receiver number 3. (b) STA/LTA ratio versus time of the data shown above. (c) Spectrogram of the data. The intensity in dB is color-coded and increases from green colors to red colors. (d) Rectilinearity versus time.

azimuth values that correspond to the second rectilinearity onset do not (indicating an S-wave with azimuths approximately 90° to the P-wave). The dip of the polarization vector at both sharp rectilinearity onsets was calculated and analyzed in relation to the corresponding receiver depth. A consistent increase in the dip values with decreasing receiver depth was observed for the first sharp rectilinearity onset. From the azimuth and dip investigations the phase identification was concluded as shown in Figure 4.12 (d).

The dominant frequency of the P-wave was approximately 100 Hz as indicated by the spectrogram analysis shown in Figure 4.11 (c) which corresponds to a dominant period of approximately 10 ms. An interval of 50-80 ms around the P-wave onset was selected (see red marked interval in Figure 4.10). This selected time interval as well as a simple 1D velocity model (Rutledge et al., 2004) which consisted of six layers were used for the location (see Figure 4.13). As described in section 3.2 the location method can be applied using selective raytracing or performing raytracing for each sample of the selected time interval. For this case study sample-by-sample raytracing and back-propagation was used to image the sources. The source image for the event shown in Figure 4.10 is shown in Figure 4.14. High energy (red to white colors) marks the hypocenter of the event. The region around the event location characterized by high stacked energy values has an elliptical shape similar to the results obtained from synthetic data with vertical

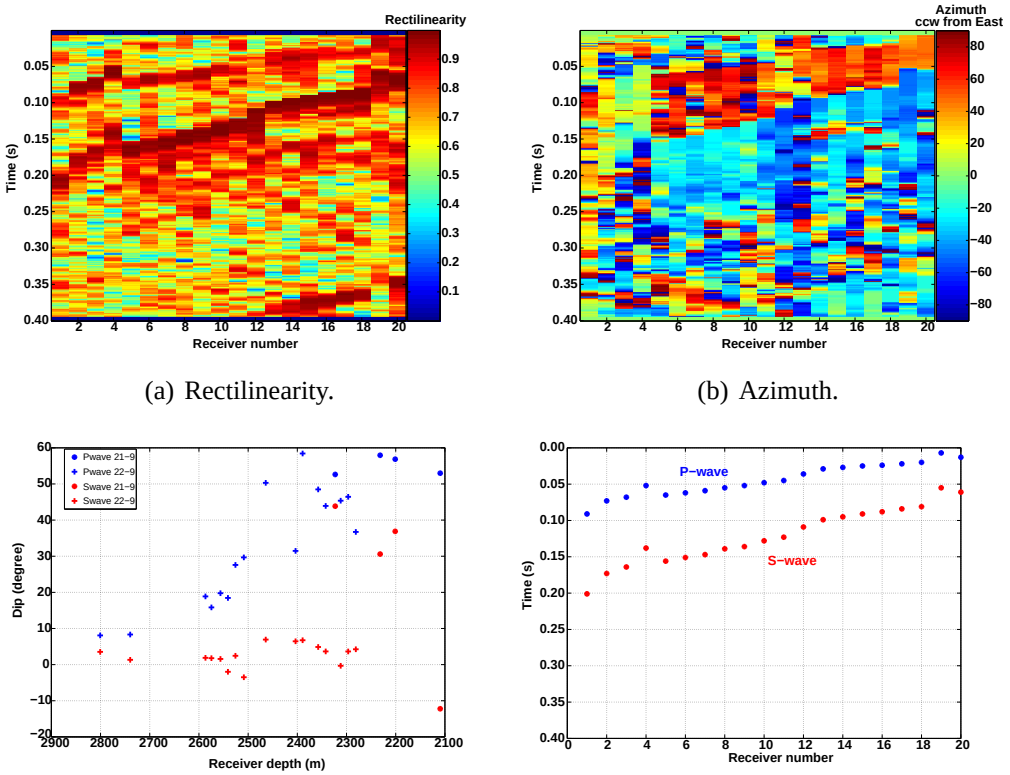

(a) Rectilinearity.

(b) Azimuth.

(c) Dip versus receiver depth.

(d) Phase detection and identification.

Figure 4.12: Scheme of phase detection and identification utilizing array-specific polarization features.

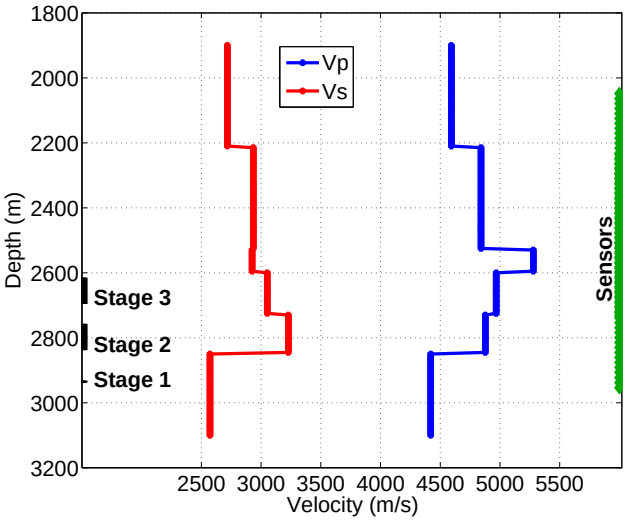

Figure 4.13: Velocity model after Rutledge et al. (2004).

array geometries (see section 3.3). Again this is caused by the receiver geometry because all rays are traced approximately in the same direction. However, the energy is strongly focusing in the final source image and indicates a reliable estimation of the hypocenter.

The location method was applied to a subset of the induced microseismic events and a comparison with different event location results from Rutledge et al. (1998), Urbancic et al. (1999) and Rutledge et al. (2004) is given in Figure 4.15. These other event locations were obtained using a variation of the Geiger method (Thurber and Rabinowitz, 2000), where P- and S-wave arrival times are required. Blue circles correspond to locations obtained by Urbancic et al. (1999) and red squares to initial event locations obtained by Rutledge et al. (1998). Rutledge et al. (2004) relocated this data set with new picks of arrival times. These locations are shown as cyan triangles in Figure 4.15. Green stars correspond to event locations obtained by the application of the location procedure presented in this work. These event locations show in general a very agreement with the results from the arrival-time-based location methods.

The uncertainty of locations obtained with the presented location method depends mainly on the signal-to-noise ratio and the quality of the receiver orientation. The S/N ratio of the event subset located here fullfilled the 9.1 dB threshold estimated in section 3.4 for a single well downhole array. Hence, the major influence comes from the receiver orientation. As mentionend before, the hodogram based receiver orientations were used whenever this information was available. Under the assumption that the horizontal receiver orientation uncertainty is in the order of 5 degrees the deviation of a ray at 400 - 500 m distance from the monitoring well can be estimated to be on the order of 40 m.

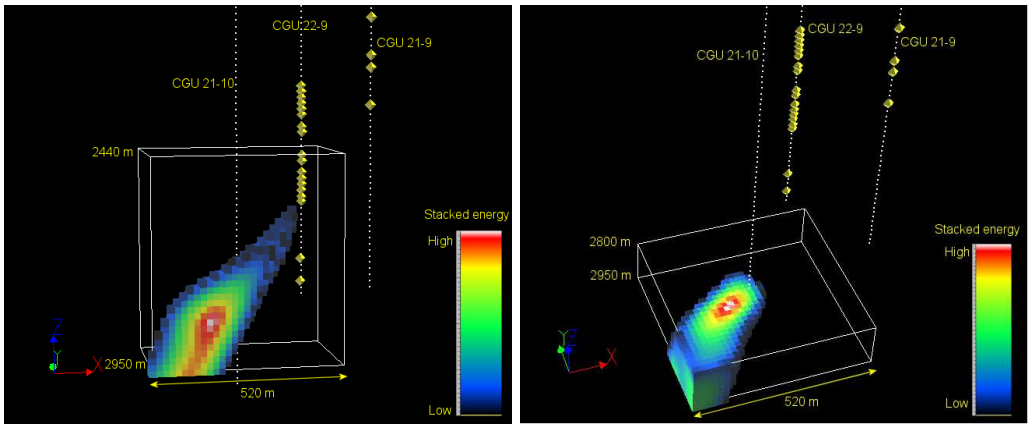

Figure 4.14: Resulting images at a slice 50 m south of the treatment well (left) and view from above at a depth of 2800 m (right). The region with maximum stacked energy (white color) marks the hypocenter of this microseismic event. Yellow diamonds mark the used receivers.

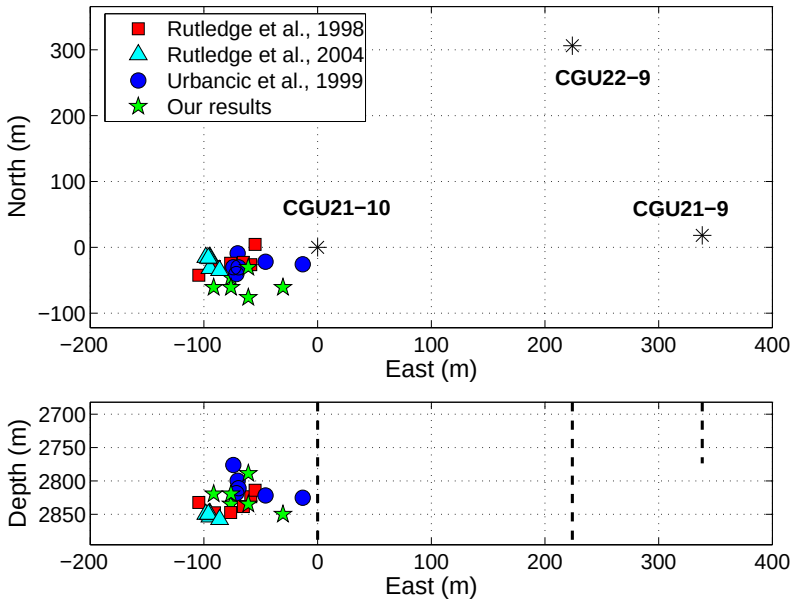

Figure 4.15: Comparison of event locations obtained by different location methods (red squares: Rutledge et al. (1998); blue circles: Urbancic et al. (1999); cyan triangles: Rutledge et al. (2004) and green stars: our approach).

4.5 Robustness tests

In order to test the robustness of the presented location method time intervals of the Carthage Cotton Valley data set were selected that do not satisfy the basic assumptions of the location approach. This means time intervals were put into the location procedure that did not contain a direct P-wave arrival. Firstly, a time interval of 100 ms was chosen that did not show any rise in the STA/LTA ratio, i.e. it did not contain any coherent arrival or, at least, none that fulfilled the S/N limits mentioned above (blue marked interval in Figure 4.16, (a)). The setup for the location algorithm was not changed, which means that the P-wave velocity model, the model dimensions and the number of receivers used for location were the same. A map view at the depth slice of the maximum energy in the resulting 3D image is shown in Figure 4.16 (c). In contrast to the image from an interval containing a direct P-wave arrival (see Figure 4.16 (b)) a clear focus of high stacked energy cannot be observed. Moreover, the time interval that contained only noise is about 50 % longer than the time interval around the direct P-wave but the highest stacked energy is about 85 % smaller than the one from the P-wave interval. For the second test a time interval of 110 ms containing a coherent arrival at the lower nine receivers of well CGU 22-9 was used (green marked interval in Figure 4.16, (a)). The resulting location image is displayed in Figure 4.16 (d), where again a map view at the depth slice of the maximum is shown. Again, the final source image does not show a distinct maximum of high stacked energy as is was observed for the interval that contained the direct P-wave. In addition, again the maximum stacked energy in this image is 80 % smaller than in the image of the P-wave interval. This means that this coherent arrival did not have polarizations pointing back and intersecting in the volume that was expected to be seismically active. In fact, this coherent arrival has its major energy on the east component and hence polarizations that point rather east-west. The corresponding rays are traced outside of the northern edge of the location model which caused some small energy artifacts along this edge. However, these artifacts along the whole edge are too small to be interpreted as a real hypocenter. Both time intervals do not satisfy the basic assumptions of the presented location method and do not produce interpretable hypocenters. This is clearly indicated by the shape of the likelihood region and by the much smaller energy values of the maxima.

4.6 Discussion

The location method presented in this thesis is especially designed for applications where real time monitoring is important, e.g. for the monitoring of hydraulic fracturing operations. The data set analyzed in this chapter was acquired during a hydraulic fracturing experiment performed in the Carthage Cotton Valley tight gas field. Encountering some problems with receiver fidelity (probably induced dur-

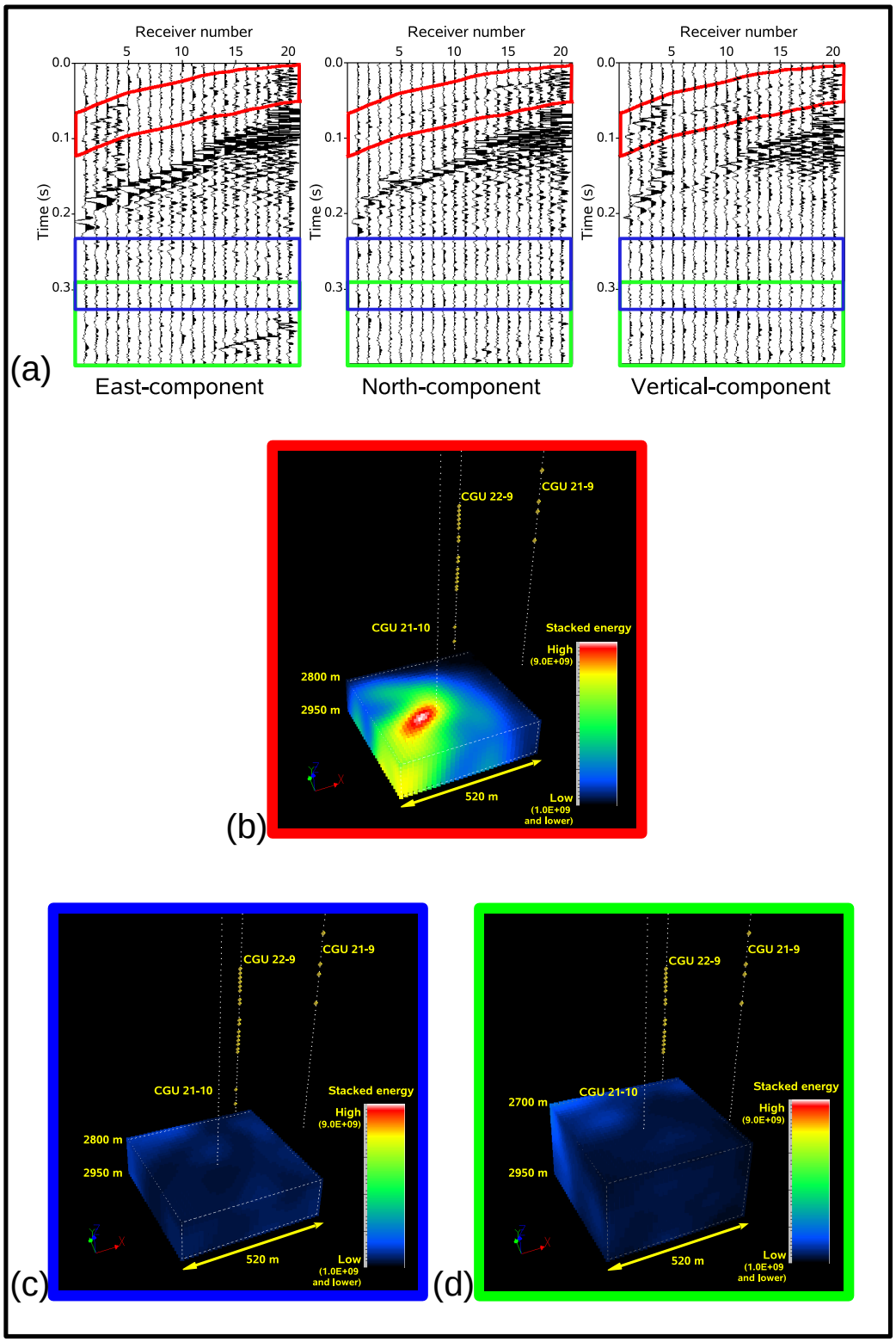

Figure 4.16: Comparison of imaging results for one time interval around the direct P-wave arrival and for two time intervals that did not fulfill the assumptions of the method. (a) 3C - data traces. (b), (c) and (d) Location image using the (red),(blue),(green) marked time intervals.

ing the deployment process) limited the number of receivers that could be used for event location. In fact, only 20 of originally 96 receivers were functioning in a way that allowed for sufficient polarization estimates. All the locations obtained using the presented location technique are in a very good agreement with its corresponding locations obtained by arrival-time based location procedures.

Furthermore, the robustness of the method was tested by applying it to time intervals of the Carthage Cotton Valley data set which did not contain a direct P-wave arrival and hence did not fulfill the basic requirements of this method. The resulting images did not produce an interpretable hypocenter and hence the method behaved robust producing zero output when using wrong data for input. This result together with the successful location of hydraulic-fracturing-induced microearthquakes supports the potential of the method for real time monitoring.

Nevertheless, it is important to note, that seismicity induced during hydraulic fracturing is characterized by its very small magnitudes. Depending on how noisy the environment is, the P-wave of the events may not always exceed the signal-to-noise limit estimated in section 3.4. The implementation of slowness driven estimates of emergence angles as well as the usage of S-wave polarization could help to increase the robustness of the location result in the case of very low signal-to-noise ratios.